Materials Innovations

Dielectric Materials | Research Article | http://doi.org/10.54738/MI.2022.2102

# Influence of Graphene Oxide on AC-conduction of Hematite Nanoparticles

**Muhammad Mumtaz**[1*], **Mubasher**[1*], **Muhammad Ali**[1], **Syed Rizwan Hussain**[2], **Muhammad Irshad Khan**[1]

**1** Department of Physics, Faculty of Basic and Applied Sciences (FBAS), International Islamic University (IIU), H10, 44000, Islamabad, Pakistan
**2** Department of Physics, School of Natural Sciences (SNS), National University of Sciences and Technology (NUST), H12, 44000, Islamabad, Pakistan

**Received:** 25 December 2021
**Accepted:** 15 January 2022
**Published:** 30 October 2022

**Citation:** Mumtaz M, Mubasher , Ali M, Hussain SR, Khan MI (**2022**) Influence of Graphene Oxide on AC-conduction of Hematite Nanoparticles. *Materials Innovations* 2 (2), 26-35.

* **Correspondences**:
(Muhammad Mumtaz)
mmumtaz75@yahoo.com
( Mubasher) mubi862008@gmail.com

Published By Hexa Publishers

**ISSN**
Electronic: 2790-1963

*The chemical sol-gel method was opted for the preparation of hematite ($\alpha$-$Fe_2O_3$) nanoparticles. The nanohybrids of graphene oxide (GO) nanosheets and $\alpha$-$Fe_2O_3$ nanoparticles {i.e. $(GO)_x/\alpha$-$Fe_2O_3$; x = 0, 0.5, 1.0 and 1.5 wt.%} were synthesized using two-step ultra-sonication method. The dispersion of GO and $\alpha$-$Fe_2O_3$ nanoparticles was done using Toluene for the preparation of $(GO)_x/\alpha$-$Fe_2O_3$ nanohybrids. The crystal structure, surface morphology and vibrational modes of these nanohybrids were studied by X-ray diffraction (XRD), scanning electron microscopy (SEM) and Fourier transform infrared spectroscopy (FTIR), respectively. XRD spectra confirmed the phase formation and rhombohedral crystal structure of $(GO)_x/\alpha$-$Fe_2O_3$ nanohybrids. The SEM images displayed that $\alpha$-$Fe_2O_3$ nanoparticles were successfully dispersed over GO nanosheets. FTIR spectra showed two transmittance bands at 464 $cm^{-1}$ and 537 $cm^{-1}$ correspond to Fe-O bond. LCR meter was used for the acquisition of frequency-dependent dielectric and impedance measurements of the samples. The variation in frequency-dependent dielectric and impedance properties was observed as GO nanosheets were hybridized with $\alpha$-$Fe_2O_3$ nanoparticles. Furthermore, the advancement in dielectric and impedance properties give evidence that the synthesized $(GO)_x/\alpha$-$Fe_2O_3$ nanohybrids could be worthy useful for high frequency devices and energy storage appliances.*

**Keywords:** Toluene, Dielectric and impedance properties, (GO)x/$\alpha$-Fe2O3, Ultra-sonication

## INTRODUCTION

The energy storage systems are experiencing remarkable improvement in order to be used to run electric trains, electric vehicles and ultimately for power grid[1–3]. The demands of material with highly optimized energy storage properties practiced substantial increase that led to extensive research on manipulation and optimization of different properties like charge storage, charge mobility and impedance of the materials[4,5]. Iron oxide is one of the most diverse materials with sixteen different types of oxide and hydroxide phases known to date. Hematite, maghemite and magnetite are the most prominent and commonly known phases of iron oxide[6,7]. The presence of octahedral or tetrahedral lattice sites in the crystal structure is a common feature of these three phases of iron oxide. The crystal structure of iron oxide can be explained in terms of the presence of iron cations on octahedral or tetrahedral interstitial sites and oxygen anions as closed packed planes[8]. Hematite ($\alpha$-$Fe_2O_3$) is one of the most stable phase of iron oxide that has hexagonal close packed arrangement of oxygen ions with Fe(III) ions occupying the octahedral sites. The $\alpha$-$Fe_2O_3$ became important material technologically because of its low cost, high stability and n-type semiconducting nature at ambient condition[9,10]. The $\alpha$-$Fe_2O_3$ shows interesting magnetic properties as it has paramagnetic nature above Curie temperature (956 K) and it remains weakly ferromagnetic on decreasing temperature from 956 K to 260 K. The $\alpha$-$Fe_2O_3$ becomes antiferromagnetic at temperatures below 260 K[11,12]. In last few decades, enormous efforts have been made to achieve the lowest possible scale for the fabrication of materials and their analysis due to emergence of striking properties with the decrease in size. The synthesis of nanostructured materials with fine size and required morphologies has always been a challenging task, especially using synthesis techniques like grinding, pressing and heating powder. The synthesis approaches such as freeze drying, high energy milling and copolymer synthesis are employed to achieve nanoscale morphologies[13–15]. Despite of enormous research on the synthesis techniques of nanomaterials, there are very few synthesis routes which are low cost and easily approachable with control over size and shape. Pertaining to the controlled size and shape, low cost chemical methods like sol-gel, co-precipitation and hydrothermal methods have proven to be successful especially for the synthesis different phases of iron oxide[14–16].

Different properties of $\alpha$-$Fe_2O_3$ nanoparticles such as non-toxicity, low-cost, bio-degradability and higher stability can be used for numerous potential applications. The extensive research has been carried out on $\alpha$-$Fe_2O_3$ nanoparticles for its potential use in applications like gas sensors, miniaturized connectors, catalysts, energy storage devices, magnetic devices, and drug delivery[16–20]. In order to find the potential applications of $\alpha$-$Fe_2O_3$ in electronic and electrical systems as well as energy storage devices, the study of dielectric properties and impedance analysis is crucial as it gives insight about charge storage, charge mobility, resistance and reactance[21,22]. The dielectric permittivity and impedance depend on many factors including phase purity, particle size and shape, charge density, temperature and pressure. The researchers are also trying to optimize the properties of $\alpha$-$Fe_2O_3$ and other phases of iron oxide through diversifying manipulation and fabrication techniques[23–26].The dielectric measurements and complex impedance spectroscopy of $\alpha$-$Fe_2O_3$ prepared by two different methods were performed. It was concluded that $\alpha$-$Fe_2O_3$ nanoparticles synthesized by precipitation method exhibited better dielectric permittivity and relaxation phenomenon[27].Mechanical and dielectric properties were found increasing for the composites of epoxy and rGO/iron oxide[28]. Mono-dispersed nanocomposites of $\alpha$-$Fe_2O_3$ with rGO were fabricated for the enhancement in wave absorption properties. The significant increase in the values of complex permittivity ($\varepsilon$) was observed for these nanocomposites that indicated excellent wave absorption properties. Furthermore, the dielectric study of $\alpha$-$Fe_2O_3$ nanoparticles indicated their potential applications in microwave application due to their low values of loss tangent[29,30].

In present study, the $(GO)_x/\alpha$-$Fe_2O_3$; x= 0, 0.5, 1.0, and 1.5 wt.% nanohybrids were synthesized by two-step ultra-sonication assisted route. Early-on, a simple and high-yield solgel method was used for the synthesis of $\alpha$-$Fe_2O_3$ nanoparticles. The $\alpha$-$Fe_2O_3$ nanoparticles and GO nanosheets were dispersed using a dispersive medium (Toluene) for these nanohybrids. The dielectric and complex impedance spectroscopic analysis response of these $(GO)_x/\alpha$-$Fe_2O_3$; x= 0, 0.5, 1.0, and 1.5 wt.% nanohybrids can guide the audience for selection of material for better energy storage devices at room temperature.

## EXPERIMENTAL SETUP

To prepare $\alpha$-$Fe_2O_3$ nanoparticles, iron nitrate ($Fe(NO_3).9H_2O$) and citric acid ($C_6H_8O_7.H_2O$) were taken in stochiometric proportion and prepared two separate solutions of both precursors. The iron nitrate was dissolved in ethanol and citric acid in distilled water with a molar ratio of 1:1, and these two solutions were homogeneously mixed by stirring. To get main solution, second solution was added in the first solution one drop wise. Ammonia was added carefully in the solution for adjustment of pH at 5. In the next step, the solution was heated at $80^oC$ for the gel formation and the solution was continuously stirred during the process. After gel formation, the sample was immediately placed in microwave oven at 100 °C for 12 h for drying. The sample was ground to get fine powder after it was removed from oven and placed in furnace in subsequent step at 500 °C for 4 h of annealing to get required $\alpha$-$Fe_2O_3$ nanoparticles. The hybridization of $\alpha$-$Fe_2O_3$ with GO was carried out by ultra-sonication method. The preparation of nanohybrids was started by taking calculated amounts of $\alpha$-$Fe_2O_3$ and GO in 50 ml of toluene, separately. Both solutions were first sonicated for 2 h using ultra-bath sonicator for uniform dispersion and then mixed. The resulting mixture was again sonicated for 6 h to disperse GO in $\alpha$-$Fe_2O_3$ homogeneously and dried for 12 h at 100 °C. The product is then subjected to annealing treatment for 1.5 h at 150 °C. After annealing, the product was again mixed mechanically to get $(GO)_x/\alpha$-$Fe_2O_3$; x= 0, 0.5, 1.0, and 1.5 wt.% nanohybrids. The phase confirmation, purity and crystal structure of $(GO)_x/\alpha$-$Fe_2O_3$ nanohybrids were determined by using XRD technique Model D/Max IIIC Rigaku with CuK source of wavelength 1.54056 Å. The SEM Model TESCANVEGA 3 with LaB6 filaments was used for morphological analysis. FTIR was employed for optical measurements from 400 cm$^{-1}$ to 700 cm$^{-1}$ range using Perklin Elmer Spectrum spectrometer. LCR meter Model Hewlett-Packard 4294A, was used for dielectric and impedance measurements in the frequency range 1 kHz to 2 MHz at room temperature.

## RESULTS AND DISCUSSION

### X-Ray Diffraction (XRD

The crystallographic and phase confirmation studies of $(GO)_x/\alpha$-$Fe_2O_3$ nanohybrids were carried out by XRD. Fig. 1a shows the representative XRD spectra of $(GO)_x/\alpha$-$Fe_2O_3$; x = 0, and 1.5 wt.% nanohybrids. All the peaks observed in XRD spectra of bare $\alpha$-$Fe_2O_3$ nanoparticles are in well agreement with rhombohedral crystal structure of $\alpha$-$Fe_2O_3$ (JCPDS Card No. 00-024-0072). The diffraction peaks corresponding to the crystallographic planes (012), (104), (110), (113), (024), (116), (214) and (300) were found at 24°, 33°, 36°, 41°, 49.6°, 54.0°, 62.5°, and 64.1°, respectively, as shown in Fig. 1. It is evident for XRD spectra that the $\alpha$-$Fe_2O_3$ nanoparticles showed high purity and excellent crystallinity. In addition, the crystallite size of $\alpha$-$Fe_2O_3$ nanoparticles was calculated by Debye-Scherrer formula and was found to be around 38 nm[31]. The GO nanosheets did not affected the crystal structure of $\alpha$-$Fe_2O_3$ nanoparticles as $(GO)_x/\alpha$-$Fe_2O_3$ nanohybrids showed identical XRD spectra as that of pure $\alpha$-$Fe_2O_3$ nanoparticles. Moreover, the GO nanosheet peaks are not observed in XRD spectra due to lower concentrations and minimal stacking of GO nanosheets[32].

### Fourier Transformed Infrared Spectroscopy (FTIR)

The vibrational modes present in $(GO)_x/\alpha$-$Fe_2O_3$ nanohybrids were investigated by FTIR spectroscopy. Fig. 1b shows the representative FTIR spectra of $(GO)_x/\alpha$-$Fe_2O_3$; x = 0, and 1.5 wt. % nanohybrids in the range from 400 cm$^{-1}$ to 900 cm$^{-1}$. FTIR verified the purity of $\alpha$-$Fe_2O_3$ nanoparticles as the present vibrational modes entirely correspond to $\alpha$-$Fe_2O_3$ and none of the bands are allocated to any impurity. In general, ferrites and other phases of iron oxide gave two separate bands for same Fe-O bond. These bands attributed to tetrahedral and octahedral lattice sites of the spinal structure. In FTIR spectra of $(GO)_x/\alpha$-$Fe_2O_3$ nanohybrids, two separate bands around 464 cm$^{-1}$ and 537 cm$^{-1}$of Fe-O bond at tetrahedral and octahedral lattice sites are observed[32,33]. GO nanosheets did not show any significant effect on FTIR spectra of nanohybrids due to their low concentration.

### Scanning Electron Microscopy (SEM)

The scanning electron microscopy (SEM) was utilized for morphological investigations of bare $\alpha$-$Fe_2O_3$ nanoparticles and $(GO)_x/\alpha$-$Fe_2O_3$ nanohybrids. The SEM images of $\alpha$-$Fe_2O_3$ nanoparticles, GO nanosheets and $(GO)_x/\alpha$-$Fe_2O_3$; x = 1.5 wt.% nanohybridare shown in Fig. 2 (a-c). The SEM image {Fig. 2(a)} confirmed the production of bare $\alpha$-$Fe_2O_3$ nanoparticles. Few agglomerations were also noticed in SEM image of $\alpha$-$Fe_2O_3$ nanoparticles. The shape and size of $\alpha$-$Fe_2O_3$ nanoparticles was not uniform though the nanostructures with flakes like shape were clearly seen in SEM images. The annealing temperature of $\alpha$-$Fe_2O_3$ nanoparticles can be the one of the possible reasons for the non-uniform size distribution as well as agglomeration and segregation of these $\alpha$-$Fe_2O_3$ nanoparticles. The SEM images of 2-dimensional GO nanosheets is presented in Fig. 2(b). The representative SEM image of $(GO)_x/\alpha$-$Fe_2O_3$; x = 1.5 wt.% nanohybrid is shown in Fig. 2(c). These SEM images showed that $\alpha$-$Fe_2O_3$ nanoparticles are evenly distributed on crumpled nanosheets of GO. Furthermore, a non-uniform and non-close packing of these $(GO)_x/\alpha$-$Fe_2O_3$ nanohybrids were also observed due to combination of two different morphologies.

### Dielectric Properties

The dielectric properties of $(GO)_x/\alpha$-$Fe_2O_3$; x = 0, 0.5, 1.0, and 1.5 wt. % nanohybrids were studied at room temperature in frequency range from 1 kHz to 2 MHz. The dielectric parameters including real part $(\varepsilon_r^{'})$ , imaginary parts $(\varepsilon_r^{''})$, tangent loss (tan$\delta$) and AC-conductivity $(\sigma_{ac})$ were calculated using standard mathematical relations[31,34]. When a material is placed between the plates of a capacitor in order to subject it to external electric field, it stores energy in the form of electric polarization. The energy stored in a dielectric is referred as real part of dielectric constant and denoted by $\varepsilon_r^{'}$'. Fig. 3a shows the variation in $\varepsilon_r^{'}$ as a function of frequency f (Hz). The dielectric response of iron oxide or ferrites is typically interpreted with the help of Koops' theory and Maxwell-Wagner model[34]. The polycrystalline materials comprised of grains and grain-boundaries. The grains have periodic arrangement of atoms in accordance with crystal structure of the material, whereas, grain-boundaries are considered as defects in crystal structure or disturbance in periodic arrangement of atoms. The conductive grains generally facilitate the flux of charges in a material, while the grain-boundaries hinder the motion of charges[35]. At low frequency, electrons flow through grains by hopping mechanism across Fe$^{+2}$

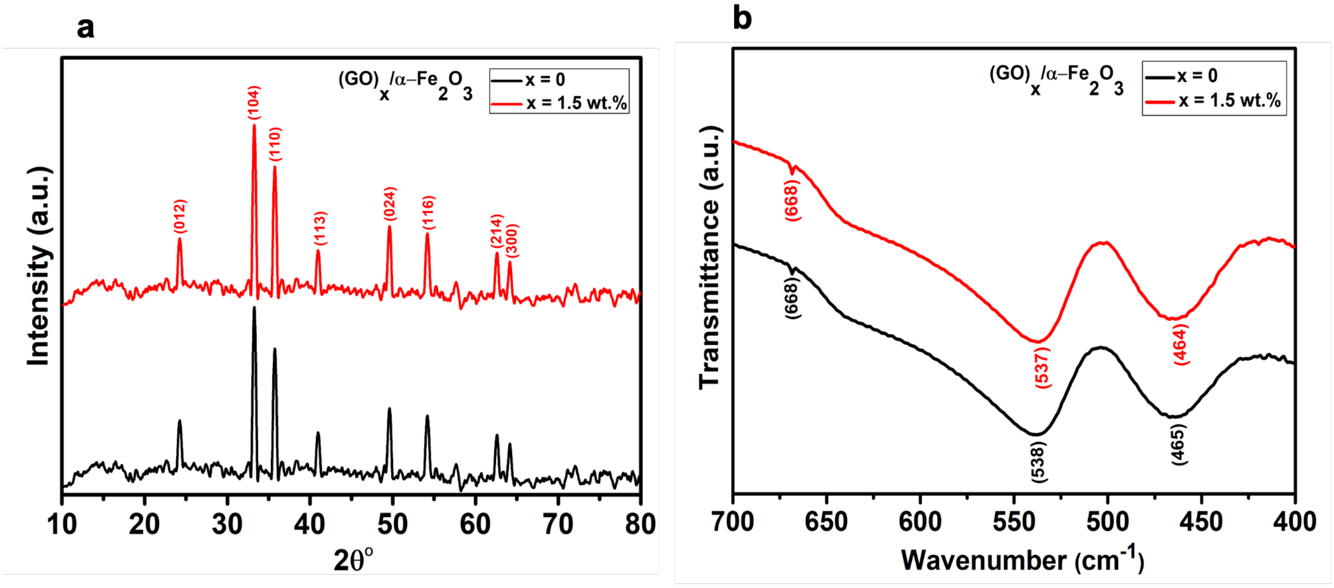

*Figure 1. (a) The representative XRD spectra of $(GO)_x/\alpha\text{-}Fe_2O_3$; x = 0, and 1.5 wt.% nanohybrids.(b)FTIR spectra of representative $(GO)_x/\alpha\text{-}Fe_2O_3$; x = 0, and 1.5 wt.% nanohybrids.*

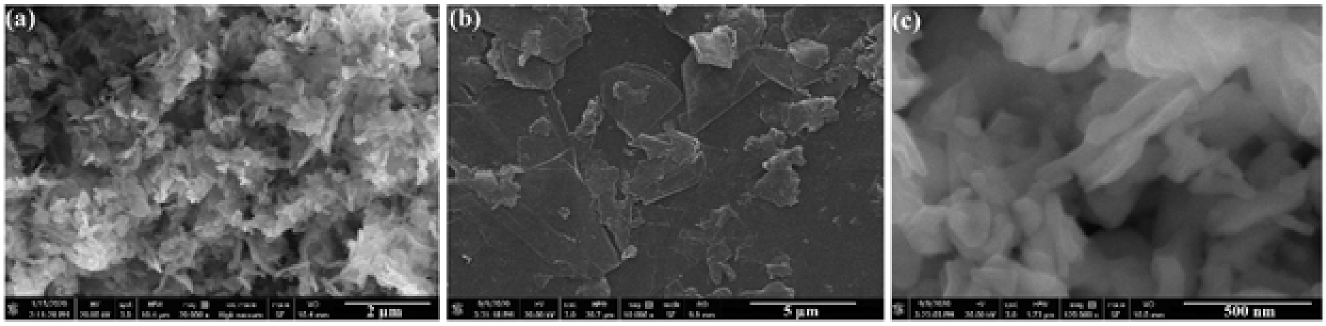

*Figure 2. (a-c): SEM images of (a) pure $\alpha\text{-}Fe_2O_3$ nanoparticles, (b)GO nanosheets and (c) representative $(GO)_x/\alpha\text{-}Fe_2O_3$;x = 1.5 wt.% nanohybrid.*

and $Fe^{+3}$ sites and got stuck and piled up across the grain-boundaries, where they cause space charge polarization resulting in higher values of $\varepsilon_r^{'}$ at low frequency[36]. At higher frequency, the electron exchange between $Fe^{+2}$ and $Fe^{+3}$ cannot follow the rapid change in AC-field due to lesser relaxation time. The large decline in $\varepsilon_r^{'}$ was observed at higher frequency as the space charges and dipoles need large time to align themselves with the high electric AC-field. When the applied frequency is further increased, the frequency of the electrons does not coincide with it, consequently, electrons stopped responding and give minimum values of $\varepsilon_r^{'}$[37]. Maximum values of $\varepsilon_r^{'}$ for $(GO)_x/\alpha\text{-}Fe_2O_3$; x = 0, 0.5, 1.0, and 1.5 nanohybrids were found to be 26.91, 6.03, 13.79, and 8.05, respectively at 1 kHz. These results illustrate that values of $\varepsilon_r^{'}$ decreased as GO is hybridized with $\alpha\text{-}Fe_2O_3$ nanoparticles.

As GO have strong chemical bonding and there are small number defects to hinder the hopping of charge carriers and their piling at grain-boundaries resulting in reduced interfacial and dipolar polarizations[38]. As a result, $\varepsilon_r^{'}$ is smaller for $(GO)_x/\alpha\text{-}Fe_2O_3$ nanohybrids than bare $\alpha\text{-}Fe_2O_3$ nanoparticles. Energy loss in a dielectric material due to free charge carriers gives imaginary part of dielectric constant commonly denoted by $\varepsilon_r^{''}$. Fig. 3b represents the plots of $\varepsilon_r^{''}$ against f (Hz)for $(GO)_x/\alpha\text{-}Fe_2O_3$; x = 0, 0.5, 1.0, and 1.5 wt.% nanohybrids. These plots demonstrate that $\varepsilon_r^{''}$ is high at low frequency and shows a decreasing trend with increasing frequency. The hopping of charges across $Fe^{+2}$ and $Fe^{+3}$ sites get higher at low frequencies due to high relaxation time of AC-field. The charges flow through grains due to hopping mechanism and piled up at grain-boundaries[35,36]. The losses of energy get higher due to highly resistive nature of grain-boundaries. Moreover, at low frequency other forms

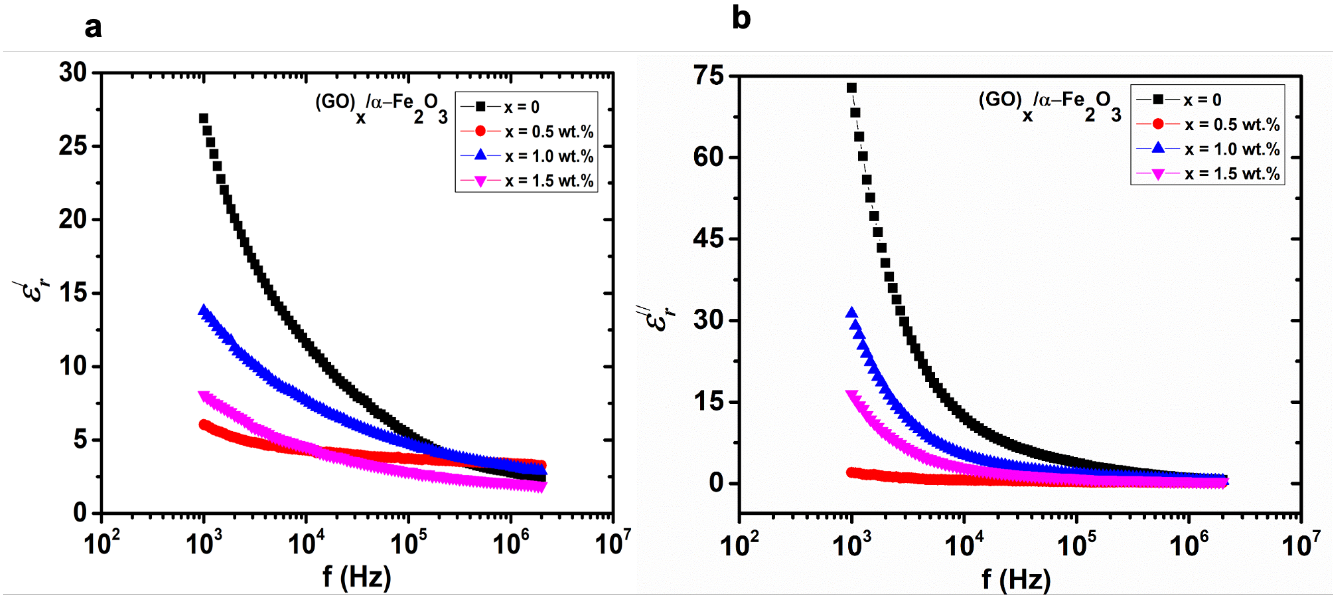

*Figure 3. (a) Real part of dielectric constant ($\varepsilon_r^{'}$) as a function of frequency f (Hz) for (GO)$_x$/α-Fe$_2$O$_3$; x = 0, 0.5, 1.0, and 1.5 wt.% nanohybrids. (b) Imaginary part of dielectric constant ($\varepsilon_r^{''}$) as a function of frequency f (Hz) for (GO)$_x$/α-Fe$_2$O$_3$; x = 0, 0.5, 1.0, and 1.5 wt.% nanohybrids.*

of polarizations are also active, which result in increase in the mobility of charges. For instance, in case of dipolar polarization, dipoles align themselves according to applied AC-field and they change their orientation frequently, which leads to more losses, so $\varepsilon_r^{''}$ shows maximum values at low frequency. At high frequency, charge carriers do not get enough energy and time for mobility to reach at grain-boundaries as result $\varepsilon_r^{''}$ is decreased at higher frequency. Maximum values of $\varepsilon_r^{''}$ for (GO)$_x$/α-Fe$_2$O$_3$ nanohybrids at x = 0, 0.5, 1.0, and 1.5 were found to be 72.85, 2.02 31.26, and 16.47, respectively at 1 kHz. It is clearly observed that (GO)$_x$/α-Fe$_2$O$_3$ nanohybrids have lesser values of $\varepsilon_r^{''}$ as compared to α-Fe$_2$O$_3$ nanoparticles due to the strong chemical bonding in GO, which can hinder the alignment of dipoles according to applied AC-field. Also, the piling of electron get reduced due to presence of GO at grain-boundaries, thus reduction in energy losses was observed.

The fractional losses in energy in a dielectric material is known as dielectric loss tangent and is denoted by $tan\delta$. Fig. 4a shows the change in $tan\delta$ of (GO)$_x$/α-Fe$_2$O$_3$; x = 0, 0.5, 1.0, and 1.5 wt.% nanohybrids with f (Hz). A declining trend with rising frequency was observed in $tan\delta$ that can be attributed to high resistance offered by grain-boundaries, which are more active at low frequency. The hopping of carriers becomes more difficult due to high resistance and more energy get consumed, which can enhance the losses in the materials. Maximum values of $tan\delta$ for (GO)$_x$/α-Fe$_2$O$_3$; x = 0, 0.5, 1.0, and 1.5 wt.% nanohybrids were found to be 2.71, 0.35, 2.11, and 1.74, respectively at 1 kHz. These values indicate that hybridization of GO with α-Fe$_2$O$_3$ hasdecreased $tan\delta$. The lesser vacancy defects of GO hinder the hopping of charge carriers, which result in smaller losses, as a result smaller values of $tan\delta$ were obtained for (GO)$_x$/α-Fe$_2$O$_3$ nanohybrids. AC-conductivity ($\sigma_{ac}$) in dielectric materials arise due flow of charges as a result of applied external electric AC-field. In iron oxide and ferrite nanoparticles, conductance of charges occurs due to hopping mechanism across Fe$^{2+}$ and Fe$^{3+}$ lattice sites.

The possibility of hopping of charge carriers across alternating tetrahedral (A-site) and octahedral (B-site) is less as compared to same B-B sites due to smaller distance between them. As a consequence of existence of hopping of electrons across octahedral lattice sites, conductance of charges is also present in α-Fe$_2$O$_3$ nanoparticles[39]. The $\sigma_{ac}$ of (GO)$_x$/α-Fe$_2$O$_3$; x = 0, 0.5, 1.0, and 1.5 wt.% nanohybrids with varying f (Hz) is shown in Fig. 4b. The trend of $\sigma_{ac}$ was increasing with increasing values of f (Hz). The mobility of charges is enhanced especially at octahedral sites at high frequency[40]. The conducting grains become more active at high frequency according to Koop's theory, so increasing trend of $\sigma_{ac}$ was observed with increasing frequency[35]. Maximum values of $\sigma_{ac}$ for (GO)$_x$/α-Fe$_2$O$_3$ nanohybrids at x = 0, 0.5, 1.0, and 1.5 were found to be $7.38\times10^{-5}$ S-m$^{-1}$, $1.54\times10^{-5}$ S-m$^{-1}$, $5.56\times10^{-5}$ S-m$^{-1}$, and $3.11\times10^{-5}$ S-m$^{-1}$, respectively at 2 MHz. It can be seen that α-Fe$_2$O$_3$ nanoparticles have high values of $\sigma_{ac}$ than (GO)$_x$/α-Fe$_2$O$_3$ nanohybrids. The

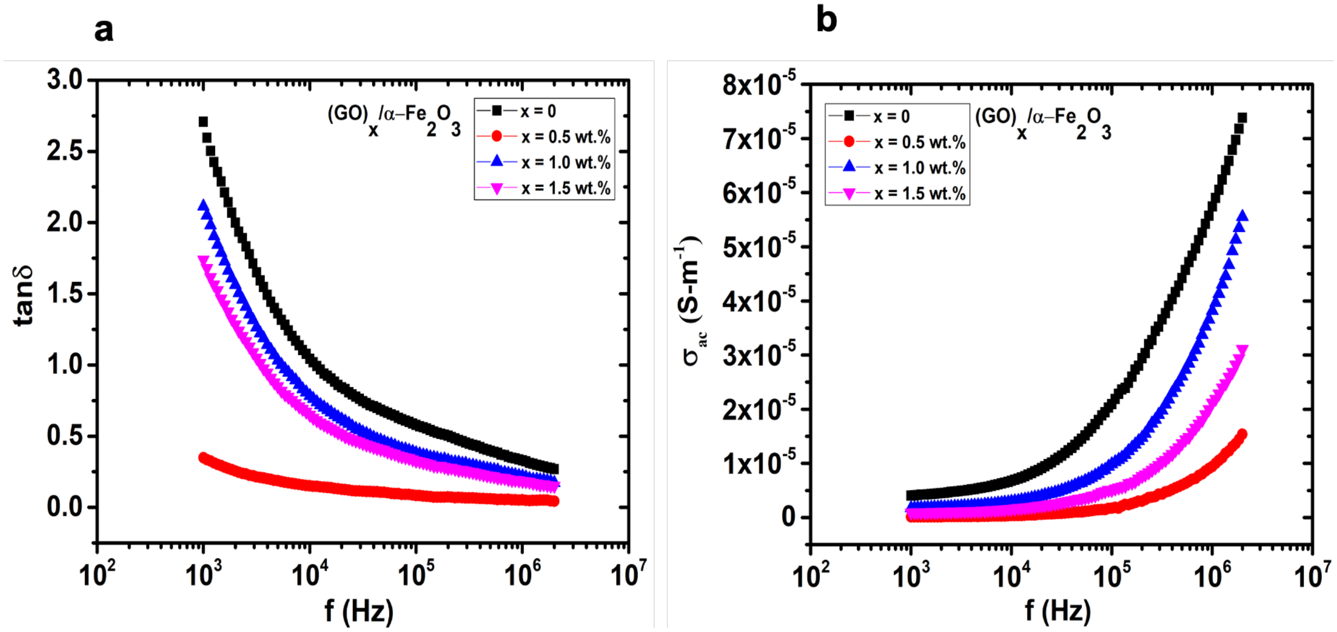

*Figure 4. (a) Tangent loss (tan$\delta$) as a function of frequency f (Hz) for $(GO)_x/\alpha\text{-}Fe_2O_3$; x = 0, 0.5, 1.0, and 1.5 wt.% nanohybrids. (b) AC-conductivity ($\sigma_{ac}$) as a function of frequency f (Hz) for $(GO)_x/\alpha\text{-}Fe_2O_3$; x = 0, 0.5, 1.0, and 1.5 wt.% nanohybrids.*

dominant factor behind AC-conduction in $\alpha\text{-}Fe_2O_3$ is hopping mechanism but the band conduction is dominant in GO for which presence of electrons in conduction band is necessary. As GO do not support hopping conduction because it does not have divalent and trivalent lattice sites like iron oxide ($Fe^{2+}$ and $Fe^{3+}$), so addition of GO suppressed the $\sigma_{ac}$ at high frequency.

## Complex Impedance Spectroscopy (CIS)

Complex impedance spectroscopy (CIS) is an important technique that is employed to study the electronic conductivity and relaxation processes in complex inhomogeneous materials. It can be used to calculate the overall resistance offered by a polycrystalline material as well as to discriminate the contributions of grains and grain-boundaries in overall resistance. From Nyquist plot of CIS, the contribution of grains and grain-boundaries in resistivity of the materials can be determined. The combined resistance of a polycrystalline material is given by $R = R_{gb} + R_g$. Thus, CIS can be used for determination and discrimination of the contribution of both grains and grain-boundaries resistances in electrical transport properties[41–43].

The variation in real part of impedance ($Z^/$) with frequency is shown in Fig. 5a. The graph illustrates that with the increasing frequency, the $Z^/$ shows a decreasing trend and becomes saturated with further increase in frequency. At low frequency, highly resistive grain-boundaries are more dominant, where charge carriers get trapped, so high values of $Z^/$ are observed[44]. But the increasing frequency results in dominance of lesser resistive grains. The charge carriers flow through the grains due to hopping mechanism between $Fe^{2+}$ and $Fe^{3+}$, so, $Z^/$ shows a decreasing trend at higher frequencies. The maximum values of $Z^/$ are $9.12\times10^6$ Ω, $1.13\times10^7$ Ω, $1.44\times10^7$ Ω, and $1.71\times10^7$ Ω at 1 kHz for $(GO)_x/\alpha\text{-}Fe_2O_3$; x = 0, 0.5, 1.0, and 1.5 wt.% nanohybrids, respectively. The hybridization of $\alpha\text{-}Fe_2O_3$ with GO resulted in enhancement of $Z^/$ in $(GO)_x/\alpha\text{-}Fe_2O_3$ nanohybrids. The enhancement in $Z^/$ can be attributed to the decrease in availability of lattice sites for hopping of charges as GO generally does not support the hopping conduction.

Fig. 5b shows the variation in imaginary part of impedance ($Z^{//}$) with frequency. The $Z^{//}$ also showed high values at lower frequency and it decreased gradually on increasing frequency. High values of $Z^{//}$ at lower frequency were due to higher relaxation time. Generally, $Z^{//}$ plots show the peaks in low frequency that indicate the presence of dielectric relaxation phenomenon. For the demonstration of peaks in this case, the plots for $Z^{//}$ can be extrapolated towards lower frequency and mobility of charge carriers occur in region below frequency range of peaks. The dispersion in peaks was also observed, which can be attributed to different relaxation behaviors of different samples. The maximum values of $Z^{//}$ were $-9.51\times10^6$ Ω, $-2.71\times10^7$ Ω, $-3.39\times10^7$ Ω, and $-4.44\times10^7$ Ω for $(GO)_x/\alpha\text{-}Fe_2O_3$; x = 0, 0.5, 1.0, and 1.5 wt.% nanohybrids, respectively.

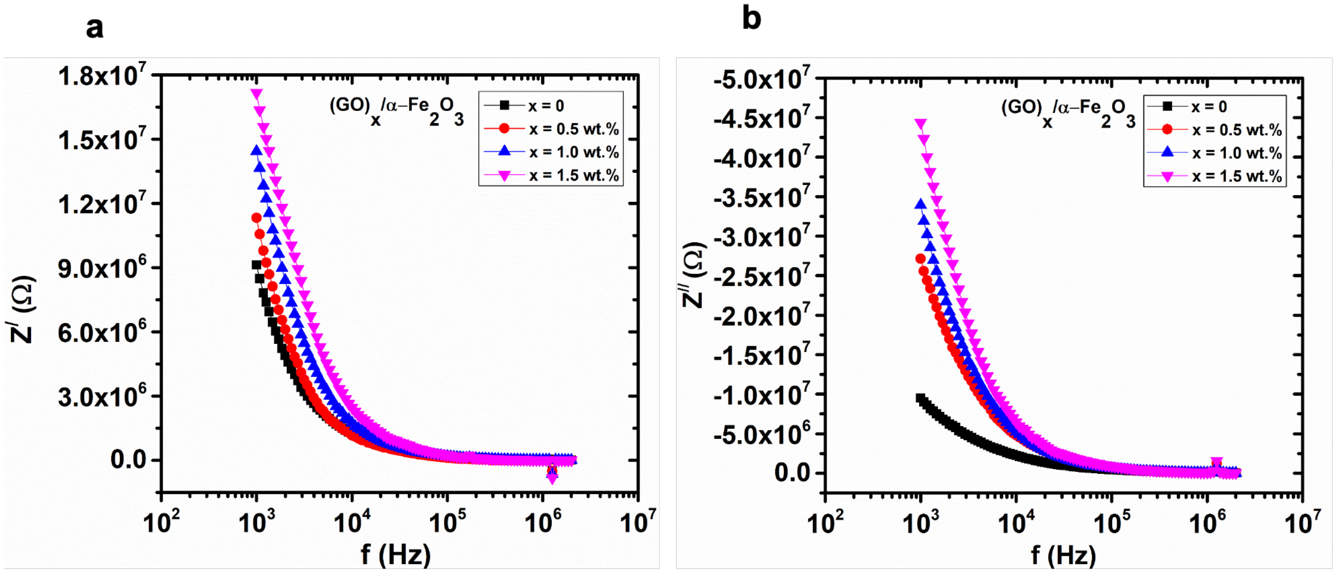

*Figure 5. (a) Real part of impedance ($Z^{/}$) as a function of frequency f (Hz) for $(GO)_x/\alpha$-$Fe_2O_3$; x = 0, 0.5, 1.0, and 1.5 wt.% nanohybrids. (b) Imaginary part of impedance ($Z^{//}$) as a function of frequency f (Hz) for $(GO)_x/\alpha$-$Fe_2O_3$; x = 0, 0.5, 1.0, and 1.5 wt.% nanohybrids.*

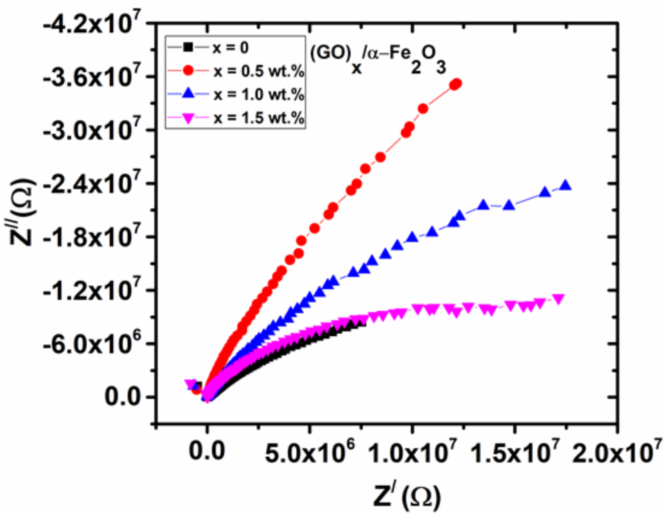

*Figure 6. Nyquist plots of impedance for $(GO)_x/\alpha$-$Fe_2O_3$; x = 0, 0.5, 1.0, and 1.5 wt.% nanohybrids.*

The Nyquist plots ($Z^{//}$vs. $Z^{/}$) for $(GO)_x/\alpha$-$Fe_2O_3$; x = 0, 0.5, 1.0, and 1.5 wt.% nanohybrids gave a semielliptical (prolonged semicircle) shape, as shown in Fig. 6, indicate the non-Debye type relaxations. The appearance of single semicircle for each sample is attributed to resistive phenomenon raised from enhanced grain-boundaries' effect[45]. The grain's resistance ($R_g$) and grain-boundaries' resistance ($R_{gb}$) were obtained from $Z^{/}$ axis of the Nyquist plots. The $R_g$ values were found to be $7.53\times10^6\,\Omega$, $1.20\times10^6\,\Omega$, $1.74\times10^7\,\Omega$, and $1.71\times10^7\,\Omega$, whereas, $R_{gb}$ values were $9.44\times10^3\,\Omega$, $2.34\times10^3\,\Omega$, $6.92\times10^3\,\Omega$, and $7.44\times10^3\,\Omega$ for $(GO)_x/\alpha$-$Fe_2O_3$; x = 0, 0.5, 1.0, and 1.5 wt.% nanohybrids, respectively. $R_g$ did not show as much change in resistance as $R_{gb}$with the hybridization of GO with $\alpha$-$Fe_2O_3$nanoparticles, while$R_{gb}$ was enhanced significantly for $(GO)_x/\alpha$-$Fe_2O_3$ nanohybrids with the addition of GO. This shows that two dimensional GO nanosheets that were present on the grain-boundaries did not allow the electron hopping. Therefore, the study helps to find out the best candidate for the fabrication of nanohybrids as anode material for batteries on the basis of dielectric properties i.e. charge storage as well as charge conduction phenomena.

## CONCLUSIONS

The preparation of $(GO)_x/\alpha$-$Fe_2O_3$; x = 0, 0.5, 1.0, and 1.5 wt.% nanohybrids was abled by using two-step synthesis route. Primarily, the chemical sol gel method was employed for the synthesis of $\alpha$-$Fe_2O_3$ nanoparticles, and then ultra-sonication assisted route was used for hybridization of $\alpha$-$Fe_2O_3$ nanoparticles on GO nanosheets, using a polar dispersive medium “Toluene”. No impurities were appeared in the XRD spectra of $(GO)_x/\alpha$-$Fe_2O_3$ nanohybrids which authenticate the successful utilization of synthesis route. The complete dispersion of $\alpha$-$Fe_2O_3$ nanoparticles over GO nanosheets was confirmed from SEM images. In FTIR spectra, transmittance bands around 464 $cm^{-1}$ and 538 $cm^{-1}$ correspond to the distinct bond lengths of Fe-O bond at octahedral and tetrahedral lattice sites of $\alpha$-$Fe_2O_3$ crystal structure. The dielectric properties were decreased with the addition of GO nanosheets in $\alpha$-$Fe_2O_3$ nanoparticles, which indicated the dominant grain-boundaries effects and reduction in vacancy defects. The increase in the impact of grain-boundaries indicated the reduction in size of grain, and increased surface area. In addition, impedance analysis indicated the presence of non-Debye type relaxation as well as an increase in resistance that attributed to the hindrance for hopping of charge carriers due to presence of GO nanosheets at the grain-boundaries. Therefore, the response of $(GO)_x/\alpha$-$Fe_2O_3$ nanohybrids in dielectric study as well as impedance spectroscopic investigations direct the audience for identification of finest material for better energy storage devices.

## References

1) Zhang, L.; Hu, X.; Wang, Z.; Ruan, J.; Ma, C.; Song, Z.; Dorrell, D. G.; Pecht, M. G. Hybrid electrochemical energy storage systems: An overview for smart grid and electrified vehicle applications. *Renewable and Sustainable Energy Reviews* **2021**, *139*, 110581–110581, DOI: 10.1016/j.rser.2020.110581, available at https://dx.doi.org/10.1016/j.rser.2020.110581.
2) Rosa, M. D.; Afanaseva, O.; Fedyukhin, A. V.; Bianco, V. Prospects and characteristics of thermal and electrochemical energy storage systems. *Journal of Energy Storage* **2021**, *44*, 103443–103443, DOI: 10.1016/j.est.2021.103443, available at https://dx.doi.org/10.1016/j.est.2021.103443.
3) Chen, M.; Zhang, Y.; Xing, G.; Chou, S.-L.; Tang, Y. Electrochemical energy storage devices working in extreme conditions. *Energy &amp; Environmental Science* **2021**, *14* (6), 3323–3351, DOI: 10.1039/d1ee00271f, available at https://dx.doi.org/10.1039/d1ee00271f.
4) Ge, G.; Huang, K.; Wu, S.; Yan, F.; Li, X.; Shen, B.; Zhai, J. Synergistic optimization of antiferroelectric ceramics with superior energy storage properties via phase structure engineering. *Energy Storage Materials* **2021**, *35*, 114–121, DOI: 10.1016/j.ensm.2020.11.006, available at https://dx.doi.org/10.1016/j.ensm.2020.11.006.
5) Abdulwahid, R. T.; Aziz, S. B.; Brza, M. A.; Kadir, M. F. Z.; Karim, W. O.; Hamsan, H. M.; Asnawi, A. S. F. M.; Abdullah, R. M.; Nofal, M. M.; Dannoun, E. M. A. Electrochemical performance of polymer blend electrolytes based on chitosan: dextran: impedance, dielectric properties, and energy storage study. *Journal of Materials Science: Materials in Electronics* **2021**, *32* (11), 14846–14862, DOI: 10.1007/s10854-021-06038-7, available at https://dx.doi.org/10.1007/s10854-021-06038-7.
6) Ramimoghadam, D.; Bagheri, S.; Hamid, S. B. A. Progress in electrochemical synthesis of magnetic iron oxide nanoparticles. *Journal of Magnetism and Magnetic Materials* **2014**, *368*, 207–229, DOI: 10.1016/j.jmmm.2014.05.015, available at https://dx.doi.org/10.1016/j.jmmm.2014.05.015.
7) Hasany, S. F.; Ahmed, I.; J, R.; Rehman, A. Systematic Review of the Preparation Techniques of Iron Oxide Magnetic Nanoparticles. *Nanoscience and Nanotechnology* **2013**, *2* (6), 148–158, DOI: 10.5923/j.nn.20120206.01, available at https://dx.doi.org/10.5923/j.nn.20120206.01.
8) Sun, S.-N.; Wei, C.; Zhu, Z.-Z.; Hou, Y.-L.; Venkatraman, S. S.; Xu, Z.-C. Magnetic iron oxide nanoparticles: Synthesis and surface coating techniques for biomedical applications. *Chinese Physics B* **2014**, *23* (3), 037503–037503, DOI: 10.1088/1674-1056/23/3/037503, available at https://dx.doi.org/10.1088/1674-1056/23/3/037503.
9) Sun, B.; Horvat, J.; Kim, H. S.; Kim, W.-S.; Ahn, J.; Wang, G. Synthesis of mesoporous $\alpha$-Fe2O3 nanostructures for highly sensitive gas sensors and high capacity anode materials in lithium ion batteries. *The Journal of Physical Chemistry C* **2010**, *114* (44), 18753–18761, DOI: 10.1021/jp102286e, available at https://dx.doi.org/10.1021/jp102286e.
10) El-Sheikh, S. M.; Harraz, F. A.; Abdel-Halim, K. S. Catalytic performance of nanostructured iron oxides synthesized by thermal decomposition technique. *Journal of Alloys and Compounds* **2009**, *487* (1-2), 716–723, DOI: 10.1016/j.jallcom.2009.08.053, available at https://dx.doi.org/10.1016/j.jallcom.2009.08.053.
11) Trpkov, D.; Panjan, M.; Kopanja, L.; Tadić, M. Hydrothermal synthesis, morphology, magnetic properties and self-assembly of hierarchical $\alpha$-Fe2O3 (hematite) mushroom-, cube- and sphere-like superstructures. *Applied Surface Science* **2018**, *457*, 427–438, DOI: 10.1016/j.apsusc.2018.06.224, available at https://dx.doi.org/10.1016/j.apsusc.2018.06.224.
12) Srivastava, M.; Ojha, A. K.; Chaubey, S.; Singh, J.; Sharma, P. K.; Pandey, A. C. Investigation on magnetic properties of $\alpha$-Fe2O3 nanoparticles synthesized under surfactant-free condition by hydrothermal process. *Journal of Alloys and Compounds* **2010**, *500* (2), 206–210, DOI: 10.1016/j.jallcom.2010.03.245, available at https://dx.doi.org/10.1016/j.jallcom.2010.03.245.
13) Hu, W.; Dong, Z.; Yu, L.; Ma, Z.; Liu, Y. Synthesis of W-Y2O3 alloys by freeze-drying and subsequent low temperature sintering: Microstructure refinement and second phase particles regulation. *Journal of Materials Science & Technology* **2020**, *36*, 84–90, DOI: 10.1016/j.jmst.2019.08.010, available at https://dx.doi.org/10.1016/j.jmst.2019.08.010.
14) Sydorchuk, V.; Vasylechko, V.; Khyzhun, O.; Gryshchouk, G.; Khalameida, S.; Vasylechko, L. Effect of high-energy milling on the structure, some physicochemical and photocatalytic properties of clinoptilolite. *Applied Catalysis A: General* **2021**, *610*, 117930–117930, DOI: 10.1016/j.apcata.2020.117930, available at https://dx.doi.org/10.1016/j.apcata.2020.117930.
15) Choudhary, A. K.; Pramanik, H. Addition of rhenium (Re) to Pt-Ru/f-MWCNT anode electrocatalysts for enhancement of ethanol electrooxidation in half cell and single direct ethanol fuel cell. *International Journal of Hydrogen Energy* **2020**, *45* (24), 13300–13321, DOI: 10.1016/j.ijhydene.2020.03.044, available at https://dx.doi.org/10.1016/j.ijhydene.2020.03.044.
16) Sun, L.; Han, X.; Liu, K.; Yin, S.; Chen, Q.; Kuang, Q.; Han, X.; Xie, Z.; Wang, C. Template-free construction of hollow $\alpha$-Fe2O3 hexagonal nanocolumn par-

ticles with an exposed special surface for advanced gas sensing properties. *Nanoscale* **2015**, *7* (21), 9416–9420, DOI: 10.1039/c5nr01790d, available at https://dx.doi.org/10.1039/c5nr01790d.

17) Hua, C.; Shang, Y.; Wang, Y.; Xu, J.; Zhang, Y.; Li, X.; Cao, A. A flexible gas sensor based on single-walled carbon nanotube-Fe2O3 composite film. *Applied Surface Science* **2017**, *405*, 405–411, DOI: 10.1016/j.apsusc.2017.01.301, available at https://dx.doi.org/10.1016/j.apsusc.2017.01.301.

18) Cho, J. S.; Hong, Y. J.; Lee, J.-H.; Kang, Y. C. Design and synthesis of micron-sized spherical aggregates composed of hollow Fe2O3 nanospheres for use in lithium-ion batteries. *Nanoscale* **2015**, *7* (18), 8361–8367, DOI: 10.1039/c5nr01391g, available at https://dx.doi.org/10.1039/c5nr01391g.

19) Tian, B.; Światowska, J.; Maurice, V.; Zanna, S.; Seyeux, A.; Marcus, P. Binary iron-chromium oxide as negative electrode for lithium-ion micro-batteries – spectroscopic and microscopic characterization. *Applied Surface Science* **2015**, *353*, 1170–1178, DOI: 10.1016/j.apsusc.2015.07.041, available at https://dx.doi.org/10.1016/j.apsusc.2015.07.041.

20) Shin, T.-H.; Choi, Y.; Kim, S.; Cheon, J. Recent advances in magnetic nanoparticle-based multi-modal imaging. *Chemical Society Reviews* **2015**, *44* (14), 4501–4516, DOI: 10.1039/c4cs00345d, available at https://dx.doi.org/10.1039/c4cs00345d.

21) Cheng, C.-J.; Lin, C.-C.; Chiang, R.-K.; Lin, C.-R.; Lyubutin, I. S.; Alkaev, E. A.; Lai, H.-Y. Synthesis of Monodisperse Magnetic Iron Oxide Nanoparticles from Submicrometer Hematite Powders. *Crystal Growth &amp; Design* **2008**, *8* (3), 877–883, DOI: 10.1021/cg0706013, available at https://dx.doi.org/10.1021/cg0706013.

22) Chi, Q.; Ma, T.; Dong, J.; Cui, Y.; Zhang, Y.; Zhang, C.; Xu, S.; Wang, X.; Lei, Q. Enhanced Thermal Conductivity and Dielectric Properties of Iron Oxide/Polyethylene Nanocomposites Induced by a Magnetic Field. *Scientific Reports* **2017**, *7* (1), 1–11, DOI: 10.1038/s41598-017-03273-z, available at https://dx.doi.org/10.1038/s41598-017-03273-z.

23) Xue, X.-Y.; Ma, C.-H.; Cui, C.-X.; Xing, L.-L. High lithium storage performance of $\alpha$-Fe2O3/graphene nanocomposites as lithium-ion battery anodes. *Solid State Sciences* **2011**, *13* (8), 1526–1530, DOI: 10.1016/j.solidstatesciences.2011.05.015, available at https://dx.doi.org/10.1016/j.solidstatesciences.2011.05.015.

24) Yan, N.; Zhou, X.; Li, Y.; Wang, F.; Zhong, H.; Wang, H.; Chen, Q. Fe2O3 Nanoparticles Wrapped in Multi-walled Carbon Nanotubes With Enhanced Lithium Storage Capability. *Scientific Reports* **2013**, *3* (1), 3392–3392, DOI: 10.1038/srep03392, available at https://dx.doi.org/10.1038/srep03392.

25) Kuang, B.; Song, W.; Ning, M.; Li, J.; Zhao, Z.; Guo, D.; Cao, M.; Jin, H. Chemical reduction dependent dielectric properties and dielectric loss mechanism of reduced graphene oxide. *Carbon* **2018**, *127*, 209–217, DOI: 10.1016/j.carbon.2017.10.092, available at https://dx.doi.org/10.1016/j.carbon.2017.10.092.

26) Sevgili, Ö.; Azizian-Kalandaragh, Y.; Altındal, Ş. Frequency and voltage dependence of electrical and dielectric properties in metal-interfacial layer-semiconductor (MIS) type structures. *Physica B: Condensed Matter* **2020**, *587*, 412122–412122, DOI: 10.1016/j.physb.2020.412122, available at https://dx.doi.org/10.1016/j.physb.2020.412122.

27) Mansour, H.; Letifi, H.; Bargougui, R.; Almeida-Didry, S. D.; Negulescu, B.; Autret-Lambert, C.; Gadri, A.; Ammar, S. Structural, optical, magnetic and electrical properties of hematite ($\alpha$-Fe2O3) nanoparticles synthesized by two methods: polyol and precipitation. *Applied Physics A* **2017**, *123* (12), 787–787, DOI: 10.1007/s00339-017-1408-1, available at https://dx.doi.org/10.1007/s00339-017-1408-1.

28) Sharmila, T. K. B.; Antony, J. V.; Jayakrishnan, M. P.; Beegum, P. M. S.; Thachil, E. T. Mechanical, thermal and dielectric properties of hybrid composites of epoxy and reduced graphene oxide/iron oxide. *Materials &amp; Design* **2016**, *90*, 66–75, DOI: 10.1016/j.matdes.2015.10.055, available at https://dx.doi.org/10.1016/j.matdes.2015.10.055.

29) Chen, D.; Wang, G.-S.; He, S.; Liu, J.; Guo, L.; Cao, M.-S. Controllable fabrication of mono-dispersed RGO–hematite nanocomposites and their enhanced wave absorption properties. *Journal of Materials Chemistry A* **2013**, *1* (19), 5996–5996, DOI: 10.1039/c3ta10664k, available at https://dx.doi.org/10.1039/c3ta10664k.

30) Qayoom, M.; Shah, K. A.; Pandit, A. H.; Firdous, A.; Dar, G. N. Dielectric and electrical studies on iron oxide ($\alpha$-Fe2O3) nanoparticles synthesized by modified solution combustion reaction for microwave applications. *Journal of Electroceramics* **2020**, *45* (1), 7–14, DOI: 10.1007/s10832-020-00219-2, available at https://dx.doi.org/10.1007/s10832-020-00219-2.

31) Mubasher,; Mumtaz, M.; Hassan, M.; Ali, L.; Ahmad, Z.; Imtiaz, M. A.; Aamir, M. F.; Rehman, A.; Nadeem, K. Comparative study of frequency-dependent dielectric properties of ferrites MFe2O4 (M=Co, Mg, Cr and Mn) nanoparticles. *Applied Physics A* **2020**, *126* (5), 1–14, DOI: 10.1007/s00339-020-03529-y, available at https://dx.doi.org/10.1007/s00339-020-03529-y.

32) Lin, L.; Pan, Q. ZnFe2O4@C/graphene nanocomposites as excellent anode materials for lithium batteries. *Journal of Materials Chemistry A* **2015**, *3* (4), 1724–1729, DOI: 10.1039/c4ta05368k, available at https://dx.doi.org/10.1039/c4ta05368k.

33) Rodulfo-Baechler, S. M.; González-Cortés, S. L.; Orozco, J.; Sagredo, V.; Fontal, B.; Mora, A. J.; Delgado, G. Characterization of modified iron catalysts by X-ray diffraction, infrared spectroscopy, magnetic susceptibility and thermogravimetric analysis. *Materials Letters* **2004**, *58* (20), 2447–2450, DOI: 10.1016/j.matlet.2004.02.032, available at https://dx.doi.org/10.1016/j.matlet.2004.02.032.

34) Ali, M.; Tehseen, U.; Ali, M.; Ali, L.; Mumtaz, M. Study of uncoated and silica-coated hematite ($\alpha$-Fe2O3) nanoparticles. *Surfaces and Interfaces* **2018**, *13*, 196–204, DOI: 10.1016/j.surfin.2018.09.011, available at https://dx.doi.org/10.1016/j.surfin.2018.09.011.

35) Saafan, S. A.; Assar, S. T. Dielectric behavior of nano-structured and bulk Li Ni Zn ferrite samples. *Journal of Magnetism and Magnetic Materials* **2012**, *324* (19), 2989–3001, DOI: 10.1016/j.jmmm.2012.04.037, available at https://dx.doi.org/10.1016/j.jmmm.2012.04.037.

36) Mazen, S. A.; Abu-Elsaad, N. I. Dielectric properties and impedance analysis of polycrystalline Li-Si ferrite prepared by high energy ball milling technique. *Journal of Magnetism and Magnetic Materials* **2017**, *442*, 72–79, DOI: 10.1016/j.jmmm.2017.06.085, available at https://dx.doi.org/10.1016/j.jmmm.2017.06.085.

37) Fadhil, A. C.; Akram, R. J.; Sabreen, A. A. Studying Dielectric and Magnetic Properties of Nano Ferrite Functionally Graded Materials. *Energy Procedia* **2017**, *119*, 52–60, DOI: 10.1016/j.egypro.2017.07.046, available at https://dx.doi.org/10.1016/j.egypro.2017.07.046.

38) Kuang, B.; Song, W.; Ning, M.; Li, J.; Zhao, Z.; Guo, D.; Cao, M.; Jin, H. Chemical reduction dependent dielectric properties and dielectric loss mechanism of reduced graphene oxide. *Carbon* **2018**, *127*, 209–217, DOI: 10.1016/j.carbon.2017.10.092, available at https://dx.doi.org/10.1016/j.carbon.2017.10.092.

39) Rahman, M. T.; Vargas, M.; Ramana, C. V. Structural characteristics, electrical conduction and dielectric properties of gadolinium substituted cobalt ferrite. *Journal of Alloys and Compounds* **2014**, *617*, 547–562, DOI: 10.1016/j.jallcom.2014.07.182, available at https://dx.doi.org/10.1016/j.jallcom.2014.07.182.

40) Sahoo, B.; Sahu, S. K.; Nayak, S.; Dhara, D.; Pramanik, P. Fabrication of magnetic mesoporous manganese ferrite nanocomposites as efficient catalyst for degradation of dye pollutants. *Catalysis Science &amp; Technology* **2012**, *2* (7), 1367–1367, DOI: 10.1039/c2cy20026k, available at https://dx.doi.org/10.1039/c2cy20026k.

41) Omari, L. H.; Moubah, R.; Boutahar, A.; Hajji, L.; Ouatib, R. E. Analysis of electrical properties using complex impedance spectroscopy in solid solutions (PbTiO3)0.97-(LaFeO3)0.03 prepared by sol-gel technique. *Journal of Electroceramics* **2020**, *44* (1-2), 23–31, DOI: 10.1007/s10832-020-00199-3, available at https://dx.doi.org/10.1007/s10832-020-00199-3.

42) Hou, J.; Vaish, R.; Qu, Y.; Krsmanovic, D.; Varma, K. B. R.; Kumar, R. V. Dielectric relaxation and electrical conductivity in Bi5NbO10 oxygen ion conductors prepared by a modified sol–gel process. *Journal of Power Sources* **2010**, *195* (9), 2613–2618, DOI: 10.1016/j.jpowsour.2009.11.081, available at https://dx.doi.org/10.1016/j.jpowsour.2009.11.081.

43) Kaiser, M. Electrical conductivity and complex electric modulus of titanium doped nickel–zinc ferrites. *Physica B: Condensed Matter* **2012**, *407* (4), 606–613.

44) Nasri, S.; Hafsia, A. L. B.; Tabellout, M.; Megdiche, M. Complex impedance, dielectric properties and electrical conduction mechanism of La0.5Ba0.5FeO3$-\delta$ perovskite oxides. *RSC Advances* **2016**, *6* (80), 76659–76665, DOI: 10.1039/c6ra10589k, available at https://dx.doi.org/10.1039/c6ra10589k.

45) Dagar, S.; Hooda, A.; Khasa, S. Dielectric properties, complex impedance analysis and electrical properties of novel particulate composites of NBT-SrFe12O19. *Journal of Materials Science: Materials in Electronics* **2020**, *31* (14), 11609–11617, DOI: 10.1007/s10854-020-03709-9, available at https://dx.doi.org/10.1007/s10854-020-03709-9.